Remote Sensing Dust Deposition by the Unique Reflectance Features of Lunar Regolith

by

Luke Johann Eberwein

An honors thesis submitted to the

Undergraduate Honors Department of the

University of Colorado in partial fulfillment of the

Honors Physics Bachelors of Arts

College of Arts and Sciences

April 2022

Thesis Advisor:

Dr. Xu Wang, LASP

Defense Date: 4/4/2022

Defense Committee:

Dr. Xu Wang, LASP

Professor Daniel Dessau, Department of Physics

Professor Kevin Manley, Department of Mathematics

Dr. Hsiang-Wen Hsu, LASP

Eberwein, Luke Johann (B.A., Physics)

Remote Sensing Dust Deposition by the Unique Reflectance Features of Lunar Regolith

Thesis directed by Dr. Xu Wang with the assistance of Dr. Hsiang-Wen Hsu.

Fine grained regolith presents a potentially hazardous problem to lunar exploration and research, and it is vital to characterize regolith mobilization on airless bodies such as the Moon. Electrostatic dust lofting has been suggested to cause observations of dust movement such as the Lunar Horizon Glow, dust ponds on the near-earth asteroid 433 Eros, and the radial spokes on Saturn's rings. Solar wind and UV radiation negatively charge the micro-cavities between dust particles. The resulting Coulomb force then overcomes the forces of gravity and cohesion, lofting the particles. Laboratory experiments have sought to characterize the launch velocities, lofting rates, and size distributions of regolith. However, without dedicated instrumentation needed to observe electrostatic dust lofting activities outside of the laboratory, a remote-sensing method may be the most feasible way to examine the possible fine grained regolith activity in situ. Our experiments seek to confirm and expand on the work of Yan et al., 2019, in which the reflectance color ratio profiles of lunar rock obtained by the Chang'E-3 Yutu rover cameras were proposed as a new identifier of dust deposition caused by electrostatic processes. Using the same color ratios, we directly compared the reflectance properties of JSC-1 lunar regolith simulant on a white background with varying dust coverage. We showed that the reflectance color ratios decrease with increasing dust coverage. Specifically, the Blue over Red ratio is most responsive to changes in dust density, whereas Blue over Green is the least responsive. Our findings agree well with the results from Yan et al., 2019. The robust correlation identified based on our controlled laboratory experiments lays the groundwork for studying dust deposition directly on airless bodies using remote sensing techniques.

Acknowledgements

I would like to thank Dr. Hsiang-Wen Hsu for providing insight into each and every aspect of this thesis, and for working around time zones and the chaos of life to ensure my success and the completion of my work. His guidance has been invaluable.

Additionally, I would like to thank my thesis advisor and CO-I at IMPACT, Dr. Xu Wang. He gave me my first job in a research environment and encouraged me to develop several skills, such as machining and CAD modeling, which I proudly claim as one of the best aspects of my education at CU. Xu has been a fantastic boss and leader, who always makes students feel welcome and valuable in the lab. I will hold my future employers to the standard of his conduct for the rest of my career.

Lastly, I would like to thank the undergraduate and graduate students, both present and former, that I have been able to work with at LASP. Their insights, camaraderie, and advice has made this thesis both possible and enjoyable.

Contents

Chapter

Tables

Table

Figures

Figure

Chapter 1

Introduction

The presence of fine-grained regolith on airless bodies (e.g., lunar dust) poses several potential issues regarding robotic and human explorations in environments such as the lunar surface. Since the Apollo era, there have been various indications of lunar dust activities. For example, the lunar horizon glow observed at the west horizon after lunar sunsets by the Surveyor 5, 6, and 7 missions is believed to be light scattering off of a cloud of micrometer-sized-dust distributed less than a meter above the lunar surface [1][2]. This dust activity may be caused by electrostatic dust lofting, where lunar dust is charged by solar ultraviolet (UV) radiation and solar wind plasma, resulting in the mobilization of fine-grained regolith on the surface of airless bodies. This was first postulated to cause the Lunar horizon glow[1] and has since been theorized to be behind Lunar Swirls [3], the unexpectedly smooth dust ponds on near-earth asteroid 433 Eros [4][5], and even the radial 'Spokes' in Saturn's rings [6][7][8][9].

In an effort to understand the nature and the dynamics of dust lofting, a patched charge model(Figure 1.2) developed from laboratory experimentation has been proposed. It suggests that a large amount of negative charge can be built up in the cavities composed of dust particles in porous regolith by the accumulation of photo-electrons from UV radiation and secondary electrons from plasma ion and electron impacts [10]. The cohesive force between particles as well as gravity bind them until they are overcome by the resulting repulsive coulomb force, which then lofts the particles instead of gently shifting the particles apart. This cavity charging scenario was confirmed experimentally [11], and the lofting rates [12], launch velocities as functions of dust size [13], and
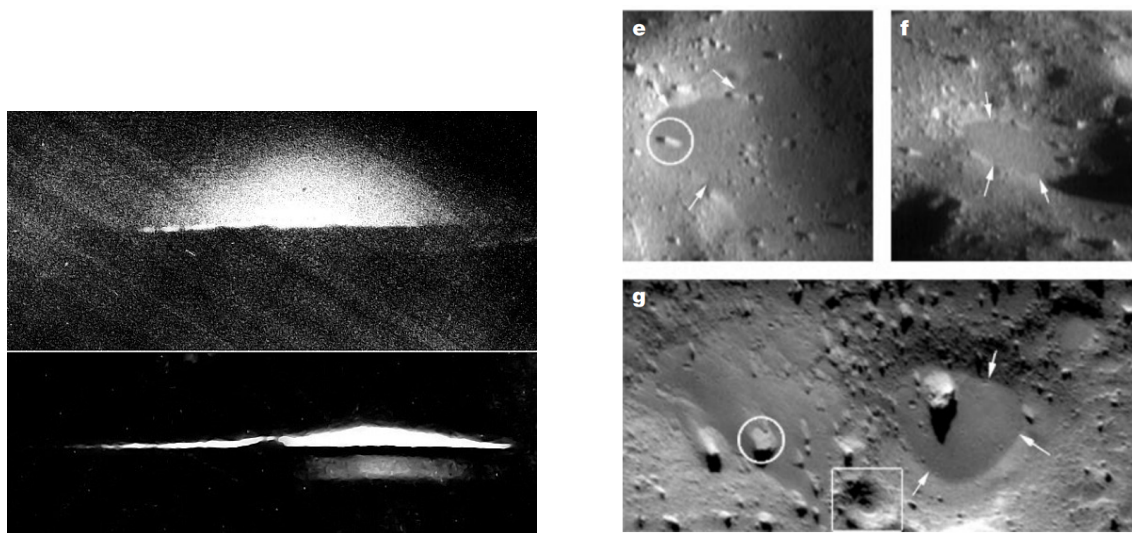
Figure 1.1: **Lunar Horizon Glow(left) and Dust Ponds on the Near-Earth Asteroid 433 Eros(right)**[4][2].
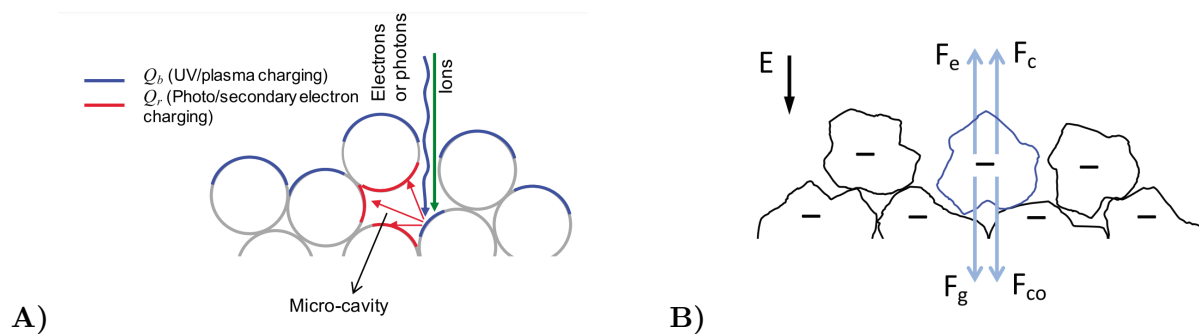
Figure 1.2: **Patched Charge Model** (A) A schematic illustration of the Patched Charge Model proposed by Wang et al., 2016 [10]. Regolith grains are charged through the collection of photo/secondary electrons induced by Solar UV and plasma within regolith micro-cavities. (B) Gravity and the cohesive force resist the plasma sheath and coulomb forces as charges build up.
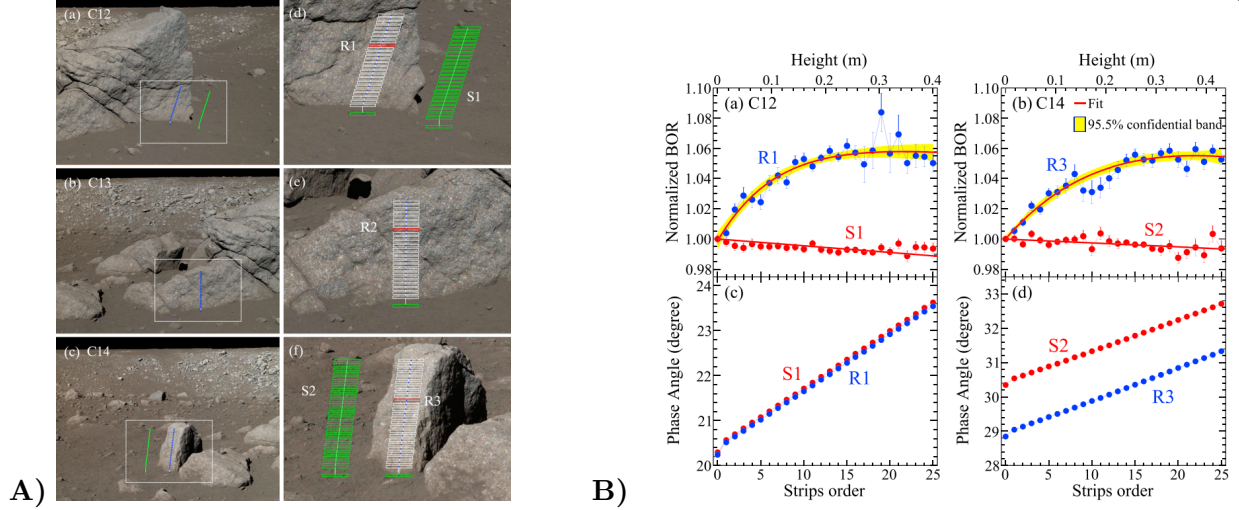
Figure 1.3: (A) Images from the Yutu Rover on the Chang'E-3 mission analyzed by Yan et al., 2019. (B) Results of the refelctance color ratios of A)a and A)c.

dust size distributions have been studied [14].

In spite of the aforementioned observations, direct evidence of electrostatic dust transport on airless bodies is still lacking. More recently, images of lunar rocks from the Yutu rover from the Chinese Chang'E-3 mission were analyzed and a new method was proposed to evaluate long-term dust activity on the lunar surface as seen in Figure 1.3[15]. In their paper they showed that the reflectance color ratio profiles along those lunar rocks vary with height from the regolith surface. The ratio profiles approach a constant value above ≈ 28 cm from the ground. This was interpreted to be evidence of electrostatically lofted near-surface dust deposition. The height of 28 cm is consistent with the altitude of the dust cloud inferred from previous lunar horizon glow and laboratory experiment results [16]. While this observation is not entirely direct evidence of electrostatic dust lofting on the Moon, it still proposes a new remote sensing method to characterize dust distribution and study the nature of dust mobilization on airless bodies.

The main goal of our work was to verify this method of using reflectance color ratios for dust detection in controlled laboratory experiments. The results from Yan et al., 2019 were strongly based on an assumption that the observed color changes were directly associated with dust de-

position. However, this remains to be verified. Our experiment compared reflectance color ratios with exact corresponding information about the location and abundance of dust coverage, and thus examined the correlation between image color ratios and dust distribution. This provides complementing results to the findings from Yan et al., 2019. In this work I establish a laboratory setup to perform reflectance measurements of dust-covered surfaces. The color values in R, G, and B bands were measured using astronomy color filters with a monochrome camera. An image analysis code was developed to calculate color ratios and examine the correlation with dust coverage derived from microscope imaging. The experimental setup and the image analysis code will be described in Chapter 2, the results and discussions will be presented in Chapter 3, and our conclusions will be discussed in Chapter 4.

Chapter 2

Experimental Setup and Data Analysis Methods

2.1 Experimental Setup

This experiment required imaging dust with a uniform background. A microscope slide was placed against a clean white plastic block as a background, and JSC-1 dust of <38 micrometers was procedurally sprinkled into 5 regions of dust density on the slide as in Figure 2.1. This dust was chosen as it is a lunar dust simulant similar to the Yan et al., 2019 imaging of real lunar dust. The small dust sticks well to the glass microscope slide. The regions(1-5, see Fig. 2.1) are about 1.5 cm wide until the last, dustless region. Region 5 had dust shaken onto it 4 times by a 38nm sieve, Region 4 had dust shaken 3 times, and so on, so that the leftmost region had no dust sprinkled onto it.

This block and slide were then placed in a chamber to block external light. Due to the configuration of the chamber's windows, two LED light sources were pointed in a converging arrangement onto the slide in the center of the chamber. Their output covers the visible light range, and so their exact irradiance by wavelength is dismissed. A commercial Astro-Photography Camera (QHY5L-II M) was used to capture each image in gray-scale, recording only the intensity of the light entering the aperture at each pixel. A filter wheel was attached between the camera and the window looking into the chamber(Figure 2.2). The filter wheel scrolls between no filter, a luminescence, red, green, and blue filter as seen in Figure 2.3.

In order to evaluate the reflectance of dust and clean surfaces, our reflectance is defined by the effectiveness of bouncing back electromagnetic power by a surface. This can be found by evaluating
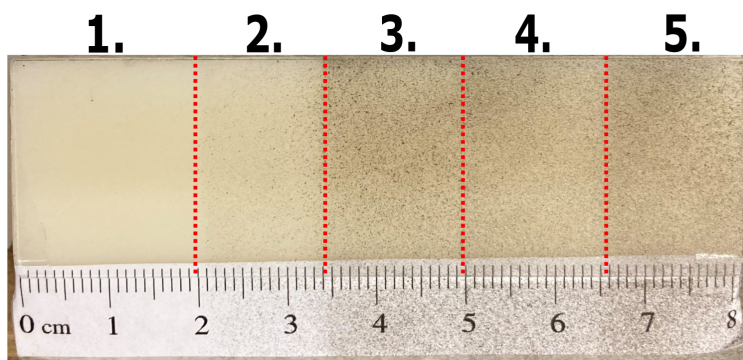
Figure 2.1: **Microscope Slide on White Plastic Block Background** Five regions of dust coverage were distributed onto the slide. From the left to right each region is labeled 1-5. A paper scale was taped to the edge to aid in conversions.
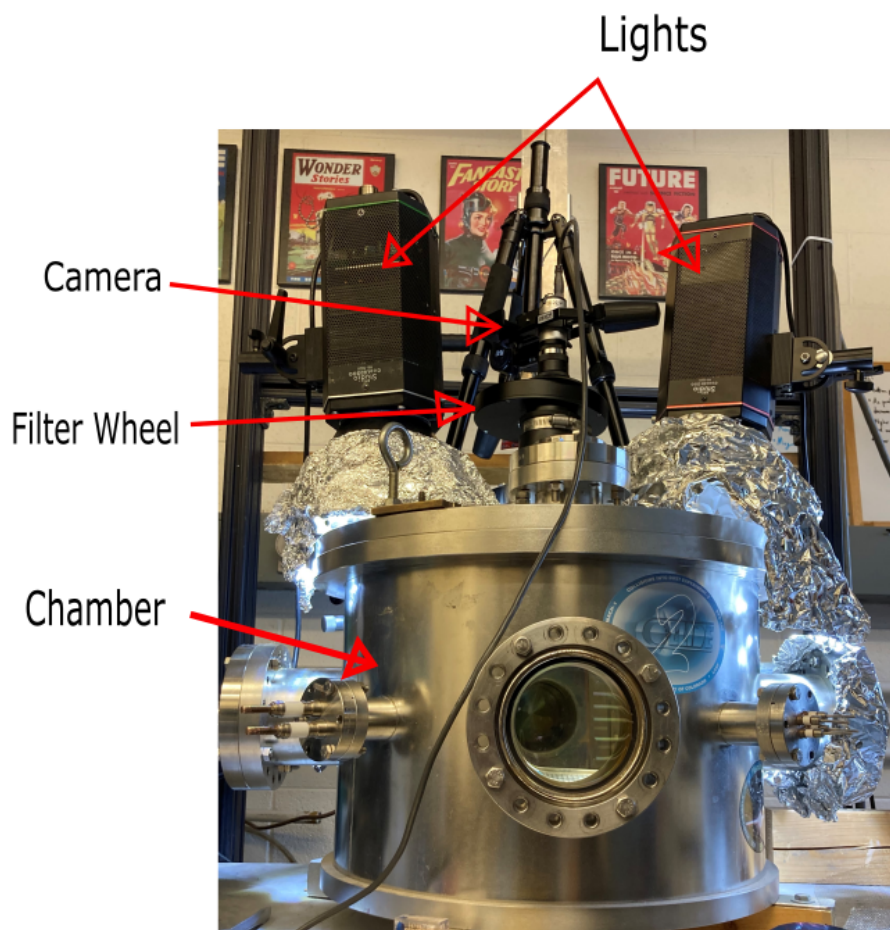
Figure 2.2: **Experimental Setup** The chamber configuration was setup to remove external light sources and to fix the positions of the lights and camera throughout data collection.

Figure 2.3: **The Filter Wheel** The lenses are reflecting light as well as transmitting and so the apparently green lens(denoted by slot 2) is the red filter, the apparently red lens(slot 3) is the green filter, and the apparently blue lens(slot 4) is indeed the blue filter. Slot 1 contains the Luminescence filter.

how light reflects from a source, off a surface, and into a camera. The intensity and wavelength of absorbed vs. reflected light depend on various properties such as particle shape, composition, and molecular structure [17]. Reflectance is given by:

$$\text{Reflectance} = \frac{\Psi_{\text{reflected}}}{\Psi_{\text{incident}}} \tag{2.1}$$

which we approximate for our experiment in Section 2.1.1. $\Psi_{\text{reflected}}$ and Ψ_{incident} represent the reflected and incoming radiance respectively. The surface covered by dust particles will have different reflectance properties from a flat surface of the same material. For our purposes, we looked at the reflectance of dust on top of a clean white plastic surface.

The camera was controlled via a laptop interface using FireCapture by Torsten Edelmann [18]. The camera's Aperture/Iris and Focus are controlled by wheels, and they were adjusted according to the set up. Finding a consistent exposure setting for each color filter, while ensuring none of the images were over- or under-exposed was difficult. The green color filter allowed much more light through than the blue and red filters. The exposure of the camera was adjusted so that the aperture was kept small, and the shutter allowed to last for 65ms. With all settings held constant, an image was taken of the dusty microscope slide though each color filter (none, Luminescent, red, green, and blue).

Figure 2.4: **Diffuse Reflectance Standard** This powder standard has a known reflectance of nearly 1.

The same setup and imaging process was then repeated but the block and slide was replaced

with a Diffuse Reflectance Standard(Figure 2.4)–a white powder surface with a known reflectivity of ≈ 0.99 at visib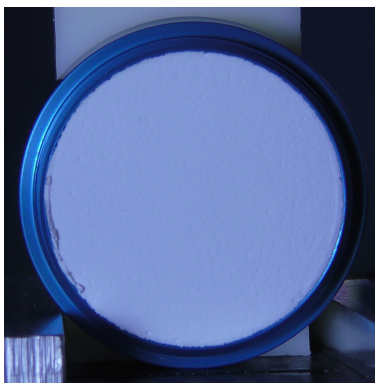le light wavelengths [19]. Because the Astro-Camera and color filters are also within the visible spectrum, the images of the standard can be treated as the incident radiance. The standard was placed at the same distance from the camera, and images were captured through the color filters with the same exposure and focus as the dusty slide images.

2.1.1   Reflectance Color Ratio Analysis

To derive the color information of dusty surfaces, an image processing code was developed to analyze the collected images described in Section 2.1. The code is written in Python, and the goal is to derive the reflectance color ratios across dusty surfaces at broadband R, G, B colors under controlled laboratory conditions. The derived reflectance color ratios were used to compare with the results presented in Yan et al., 2019.

Reflectance is defined by Equation 2.1, but for our experiment we worked with the directional reflectance which depends on the direction of both the reflected and incident radiance. We can approximate:

$$\text{Directional Reflectance} = \frac{L_\text{reflected}}{L_\text{incident}} \approx \frac{I_\text{dust}}{I_\text{standard}} \tag{2.2}$$

where $L_\text{reflected}$ is the directional radiance reflected, L_incident is the directional radiance received, and I_dust is the radiance reflected off of the dust covered microscope slide in the direction of and recorded by the camera. I_standard is the radiance reflected by the standard powder which has a known reflectance ≈ 0.99 as mentioned. This directional reflection off of a surface with a near perfect reflectivity can then be approximated to equal the incoming directional radiance.

Because our light sources were symmetrically arranged around the microscope slide and the camera directly above it, we chose not to explore the plausible effects of the light sources' phase angle and keep the angle fixed.

Two sets of images were captured using the three R, G, and B color filters. One set imaged dust on the microscope slide with a solid white background, and another set imaged the reflectance standard.
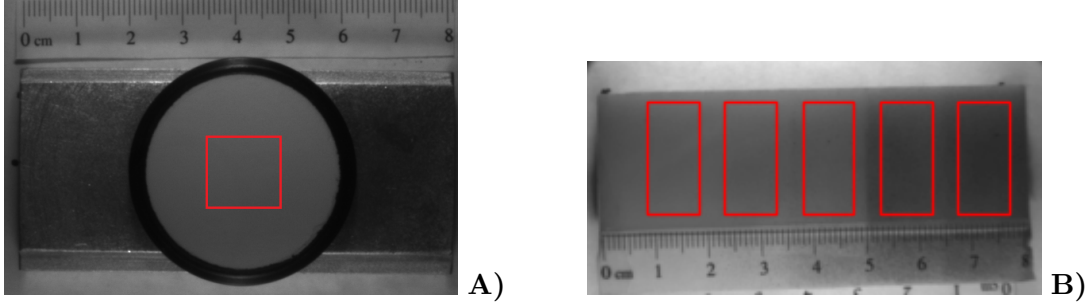
Figure 2.5: **The Captured Images** Captured in monochromatic, there are three of each these images, one for each color filter. (A) shows the section scanned of the diffuse standard image. (B) shows the sections scanned on the dust covered microscope slide. These sections are adjustable and are shown by the red boxes.

A section of pixels was selected from the center of each standard image(Figure 2.5A) and stored sequentially in a new single 1D array.(This section's size is adjustable in the code) This was then converted into a 2D array with each different filter having its own row.

This same procedure was repeated for the dust images taken with color filters, where the section wasn't selected from the center but rather at a varying positions along the x-axis (Figure 2.5B). Within the loop the 2D arrays were split into 6 separate arrays for each image, and then the dust arrays were normalized to garner the reflectance by dividing them by their respective color standard arrays according to Equation 2.2 in the form:

$$R_{\text{reflectance}} = \frac{\text{Red}_{\text{Dust Array}}}{\text{Red}_{\text{Standard Array}}} \tag{2.3}$$

Ratios of the reflectances were then obtained by:

$$\text{BoR} = \frac{B_{\text{reflectance}}}{R_{\text{reflectance}}}, \ \text{BoG} = \frac{B_{\text{reflectance}}}{G_{\text{reflectance}}}, \ \text{GoR} = \frac{G_{\text{reflectance}}}{R_{\text{reflectance}}} \tag{2.4}$$

These Ratios were chosen to match the ratios used in Yan et al. (2019). These ratio arrays were then averaged to obtain a single value corresponding to the section examined. Each iteration of the loop then stored these ratio values for each x coordinate in 1D arrays BoRdata, BoGdata, and GoRdata. The derived color ratios are then plotted with the x coordinate of the center of each section scanned as shown in Figure 2.5.

2.1.2 Dust Surface Coverage Analysis

To verify the trends of the color ratios with respect to dust density, the actual surface dust coverage was evaluated along the microscope slide. Images were taken through a microscope at several positions along the slide(Figure 2.6), with the exact position along the slide recorded for each microscopic image. Three to four images were taken for each region.
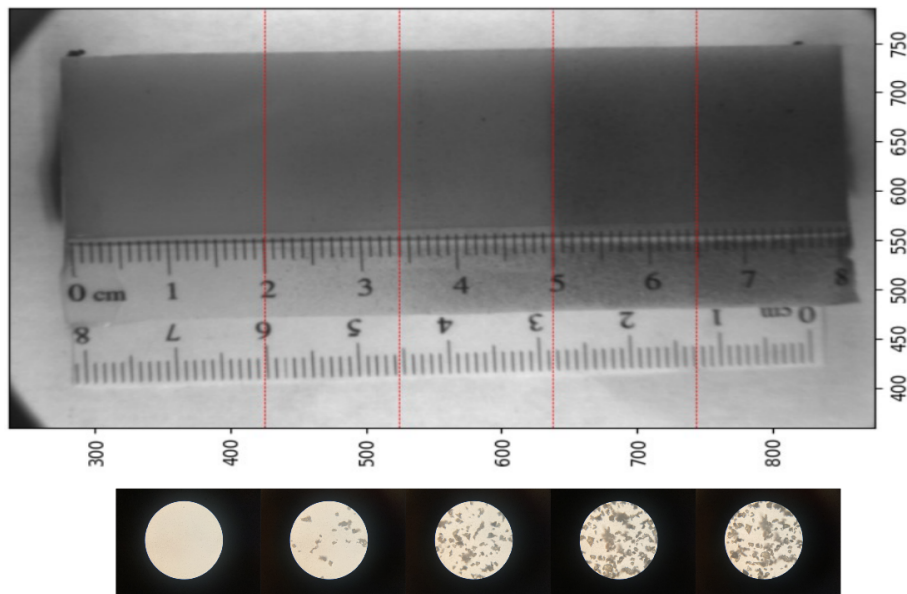
Figure 2.6: **Sample Microscope Images** Each Microscopic image captures a small area along the slide at 40x magnification. The dotted red lines show the regions of different dustiness and a sample microscope image is pictured for each region. The ruler scale attached at the bottom was used to aid in length conversions.

The microscope image analysis code used here is a modified version of code developed by Noah Hood [14]. Each image is converted to binary with a threshold value that sets pixels corresponding to dust to black, and everything else to white. Some noise is filtered and corrected, and then the percentage of surface dust coverage is calculated for each image by evaluating the amount of dust pixels per the pixels in the circular images(see Figure 2.7). These "densities" are then plotted vs the length of the slide in Fig. 2.6.
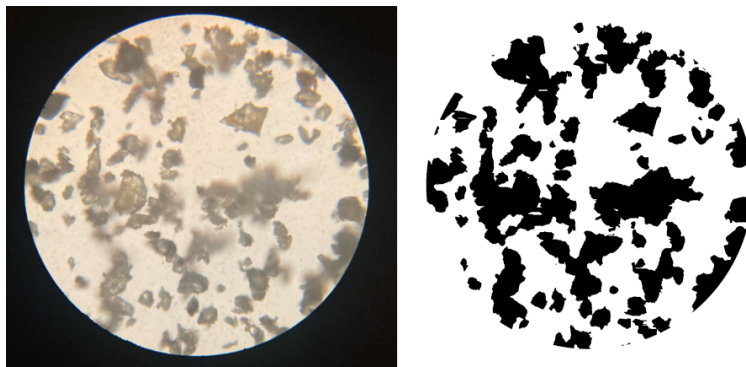
Figure 2.7: **Microscopic Image Conversion to Binary** Every microscope image is converted to binary as shown on the right. The number of black pixels per the total pixels in the circular area represents the dust density as a percentage.

Chapter 3

Results and Discussion

The images obtained using the R, G, and B filters were processed as described in Ch. 2.1.1. The derived reflectance color ratios BoR, BoG, and GoR, the dust coverage along the slide, and the sections evaluated are shown in Figure 3.1. The color ratios were calculated using the average values of each section, 150 x 10 pixels in size, shown as red boxes in Figure 3.1. In our setup, the slide was divided into 5 regions with a span of about 1.5 cm. The least dusty region appears at the left of the microscope slide and is labeled Region 1. More dust is present in each following region, with the most dust present in Region 5 as can be seen with the darker shading. The regions appear along the microscope slide roughly as in Table 3.1. The plot ranges from 340 to 845 pixels, and this length corresponds to about 7.2 cm.

Region	Pixel Range
Region 1	281 to 432
Region 2	432 to 531
Region 3	531 to 635
Region 4	635 to 743
Region 5	743 to 854

Table 3.1: **Range of Dust Regions** Given in pixels, this table shows x coordinates of Regions 1-5.

3.1　Reflectance Color Ratio Results

Figure 3.1 shows the ratio profiles of 150 by 10 pixel sections taken along the image, and shows the trend of the averaged color ratios for each section. The graph reads from left to right of

Figure 3.1: **Reflectance Ratios of 150 by 10 box sections.** 150 by 10 pixel sections are evaluated with a step size of 5 p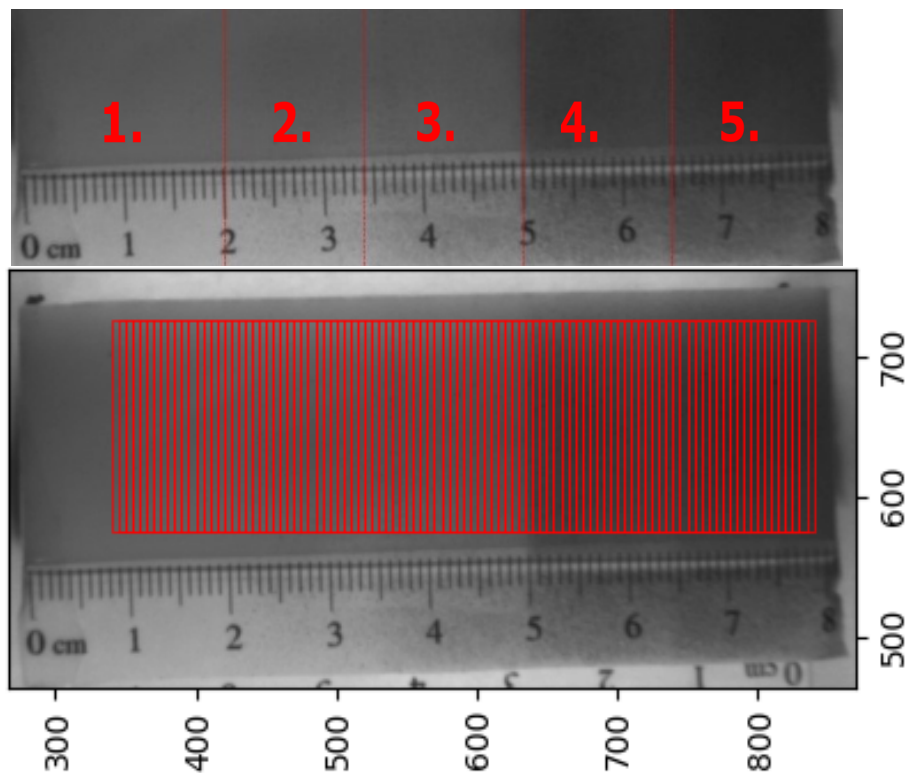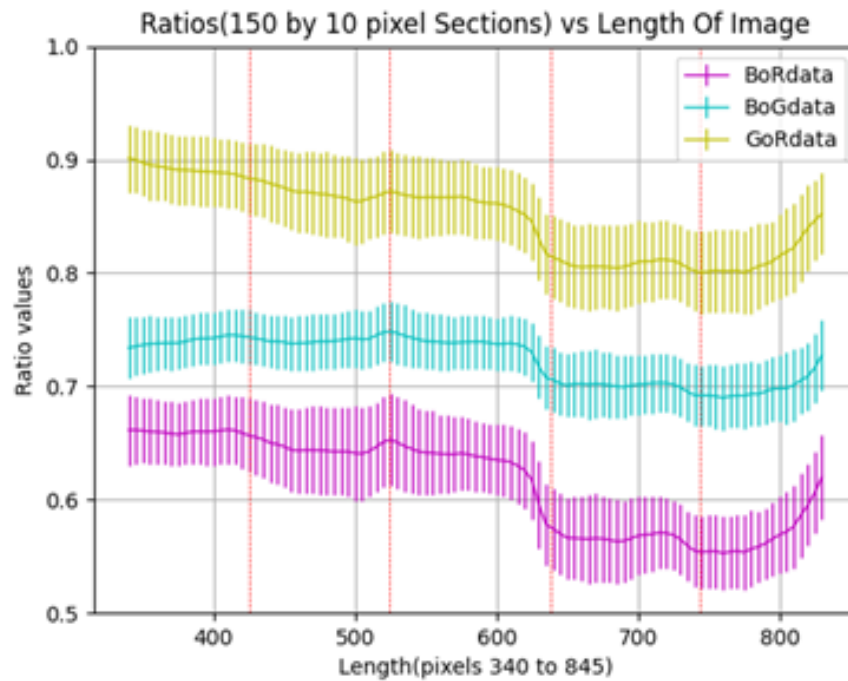ixels between their origins. The red dotted lines mark dust coverage regions and are labeled 1-5 below. The bottom image shows the overlapping sections.

the image and shows that, towards the right of the image, corresponding to more dust coverage, color ratio values are significantly lower than unity. Region 1, which is clear of dust, has the highest ratio values approaching unity. The error bars on the plot in Figure 3.1 mark the color ratio standard deviation in each section. Note that the elevated color ratios in Region 5 from about 770 to 845 pixels are likely caused by the imperfect calibration of our imaging system, e.g., the vignetting of the camera lens, but is also correlated to a possible decrease in density which can be seen in Figure 3.4.

The reflectance color ratio represents some information about the shape of the reflectance spectrum. The reflectance spectrum of the JSC-1 lunar simulant is reported by Gaier et al., 2011, and is shown in Figure 3.2a. In the visible light wavelength range (400-700 nm), the spectrum shows the highest reflectance in red, and the lowest reflectance in blue. Because of the positive spectra slope (i.e., the reflectance increases with wavelength) all the JSC-1 color ratios are expected to be lower than unity, with BoR having the lowest values, and GoR the highest. Both expectations qualitatively agree with our results as seen in Figure 3.1.

Note that the size of the JSC-1 dust samples used by Gaier et al. 2011 were <20 μm and ours were <38 μm. Also, the illumination configuration of our experimental setup likely differs from theirs. Nevertheless, while these two factors will alter specific values, the qualitative agreements between the measured color ratios and the reflectance spectrum from Gaier et al., 2011 provide validation of our measurement and analysis techniques.

The BoR and GoR ratios show a clear response to the changes in dust coverage along the length of the microscope slide, while the trend in the BoG ratio is least pronounced. One likely cause of these different responses arises from the overlap of light transmission windows of the color filters. The bandpass of the R filter does not overlap with the other two, which is not the case for the B and G filters (Figure 3.2b) [20]. This also agrees with Yan et al. 2019, where they explored the same phenomena.

"Normalized BOR shows larger variation than the normalized BOG and GOR due to the fact that the response functions of the blue and the red bands are distinctly
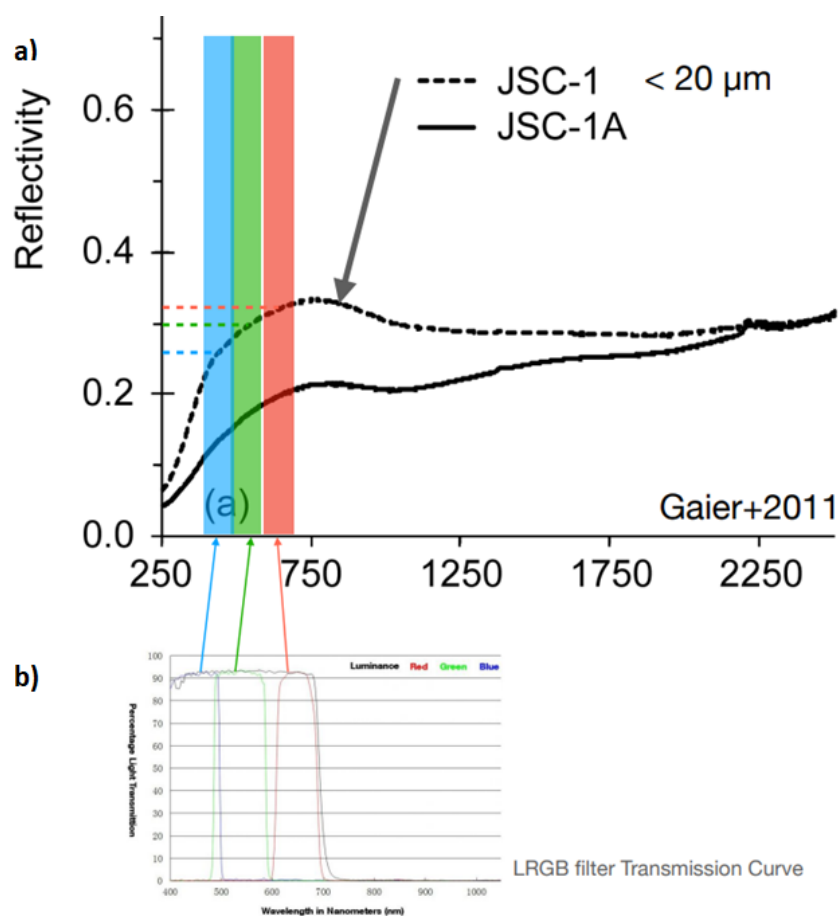
Figure 3.2: **Reflectance Spectrum of JSC-1 lunar simulant and the filter transmission range.** a) The reflectance spectra of the JSC-1 and JSC-1A lunar simulant (grain size < 20 µm) from Gaier et al., 2011. b) The transmission wavelength ranges of the R, G, and B filters used in this work.

separated with a quite small overlap between them (Ren et al., 2014)".

Note that their color information was not derived using color filters but simply derived from the Bayer filter on the image sensor. Regardless, there was a noted overlap in the wavelengths picked up by the green and blue bands.[21]

In evaluating our results, we also explored how the standard deviation changes with the dust deposition. Because the dust coverage is inhomogeneous within each 150x10 pixel section, the standard deviation likely reflects the presence of "dust specks" at local scales. However, in Figure 3.3 one can see the deviations are lowest where there is little to no dust (i.e., Regions 1-2), and highest in the middle of the slide where there are sprinklings of dust. The deviations in Region 5 decreases slightly, as the dust coverage forms a more even coating, and so yields a more consistent reflectance across the slide. This suggests that an even coating or a lack of a material on a solid color background should yield smaller standard deviation in color ratios. This was also observed by Yan et al., 2019. They found the deviation of an area of pure regolith to be small. But as the dust coverage decreases with height in their images, the deviations increase as more background is revealed.

The low responsivity of the BoG ratio is highlighted by the small deviations in Figure 3.3. Whereas the BoR and GoR deviations scatter much more with changes in dust density, BoG may have the smallest standard deviations due to the previously mentioned spectral properties of JSC-1 dust.

3.2   Dust Deposition Density Results

To provide a quantitative understanding about the trends of reflectance color ratios and dust coverage, the surface dust density was derived with microscopic imaging in each region as described in Section 2.1.2. The density is measured by the number of pixels corresponding to dust per the number of pixels in a captured microscopic image. Four images were taken in the Regions 1 and 2 (i.e., the least dusty regions), three images in Region 3, four in Region 4, and three in the dustiest
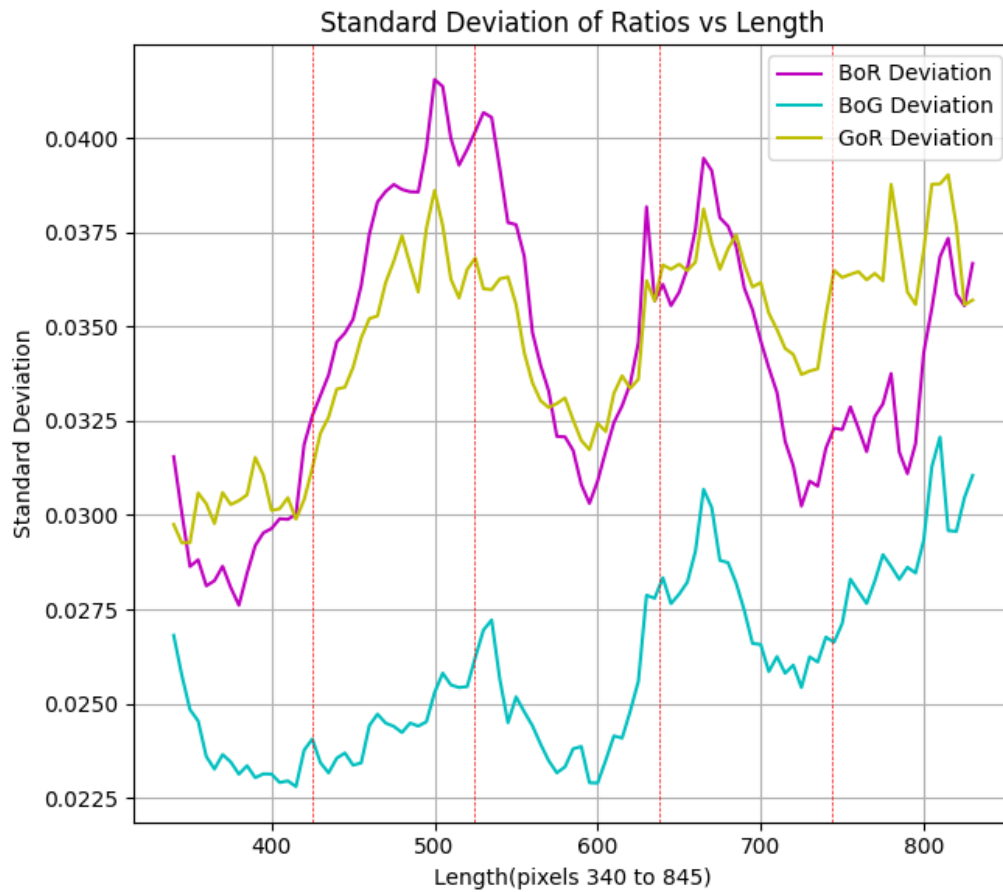
Figure 3.3: **Standard Deviations of Reflectance Color Ratios.** The standard deviation of each section along the dust-covered microscope slide.
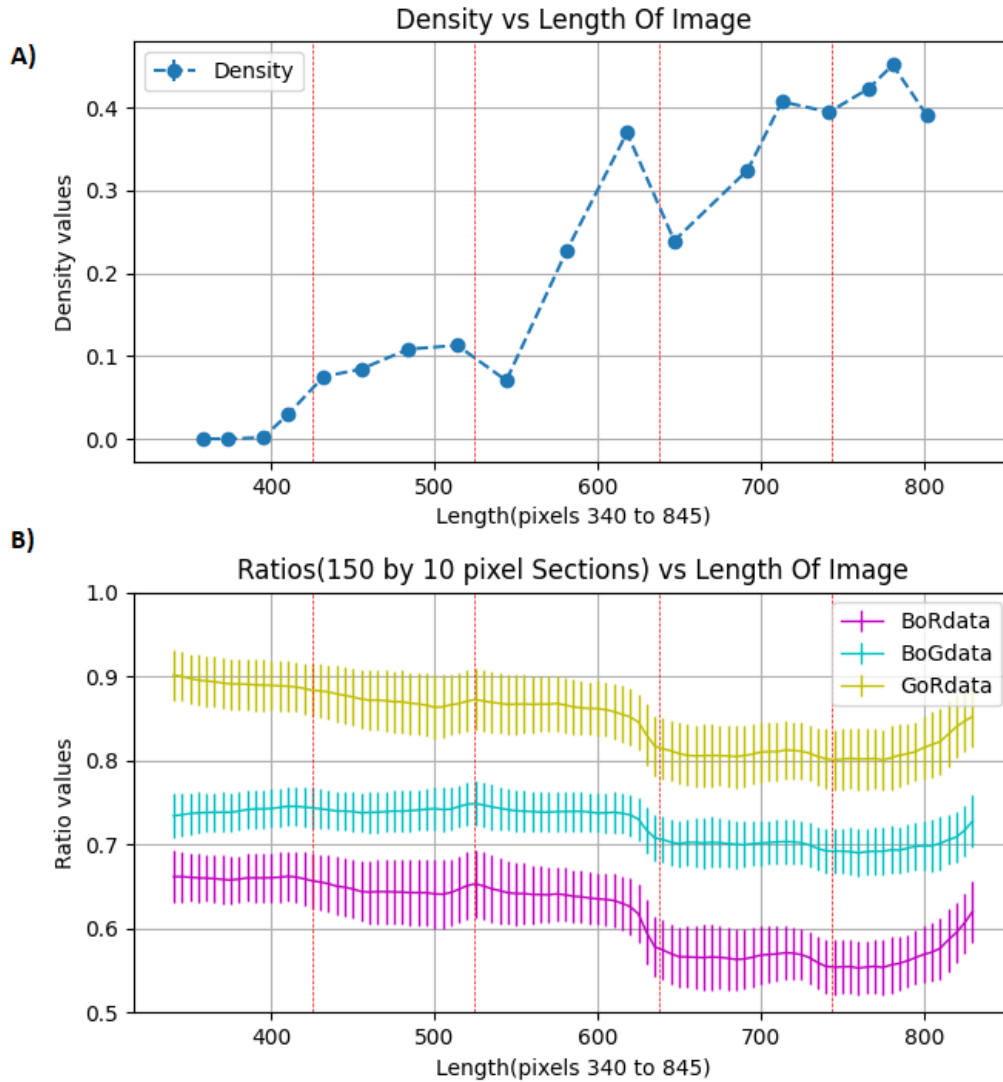
Figure 3.4: **The Dust Surface Density(Percentage of Area Covered in Dust) Compared to Reflectance Ratios.** A) The dust surface density at locations along the slide were evaluated with microscope imaging and compared with the color ratios, B), to confirm the trend. The red dotted lines show the boundary lines between regions of increasing dustiness along the slide.

Region 5.

Figure 3.4 clearly shows that the color ratios, especially BoR and GoR, decrease as dust surface density increases. Even small changes in the ratio profiles are reflected by the density around x=524. The increase in ratios at the end of the slide near x=850 matches the density decrease as well. The density points between x= 524 and 638 have a high standard deviation, which fits in to the irregularity of such small areas being evaluated under the microscope. At these middle regions, the dust distribution at local scales is much more irregular, as discussed with Figure 3.3, and the microscope images can introduce biases because of their small coverage. The situation is less severe in regions with the least and most dust, where the dust surface density is expected to be more regularly dispersed. Note the sharp increase in density near x=600 is likely statistical error due to the inhomogeneity of density, whereas the sharp drop in ratios near x=630 corresponds to the boundary of Regions 3 and 4 where dust coverage increases dramatically(see Figure 2.6). This density change is not well reflected by Figure 3.4A.

When looking at the general trends, evaluating the mean values for each region of dustiness grants a better understanding of the trend of reflectance ratios and dust density. In Figure 3.5, the dust surface coverage of Regions 1 to 5 are 0.86%, 9.56%, 22.36%, 34.16%, and 42.26%, respectively. The reflectance ratio values for each region are as shown in Table 3.2

Region	BoR Ratio	BoR std. dev.	BoG Ratio	BoG std. dev.	GoR Ratio	GoR std. dev.	Dust Density	Density std. dev.
Region 1	0.66	0.03	0.74	0.02	0.90	0.03	0.8%	1%
Region 2	0.65	0.04	0.74	0.02	0.87	0.04	9.5%	2%
Region 3	0.64	0.03	0.74	0.02	0.87	0.03	22.2%	15%
Region 4	0.57	0.04	0.70	0.03	0.81	0.04	34.1%	8%
Region 5	0.57	0.04	0.70	0.03	0.82	0.04	42.2%	3%

Table 3.2: **Reflectance Ratios for each Dust Region** The mean values of the reflectance color ratios for the five regions

The trend of Figure 3.5 shows a decrease in ratio values with increasing dust density. The density's large standard deviation in Region 3 corresponds to the biases and inhomogeneity in dust
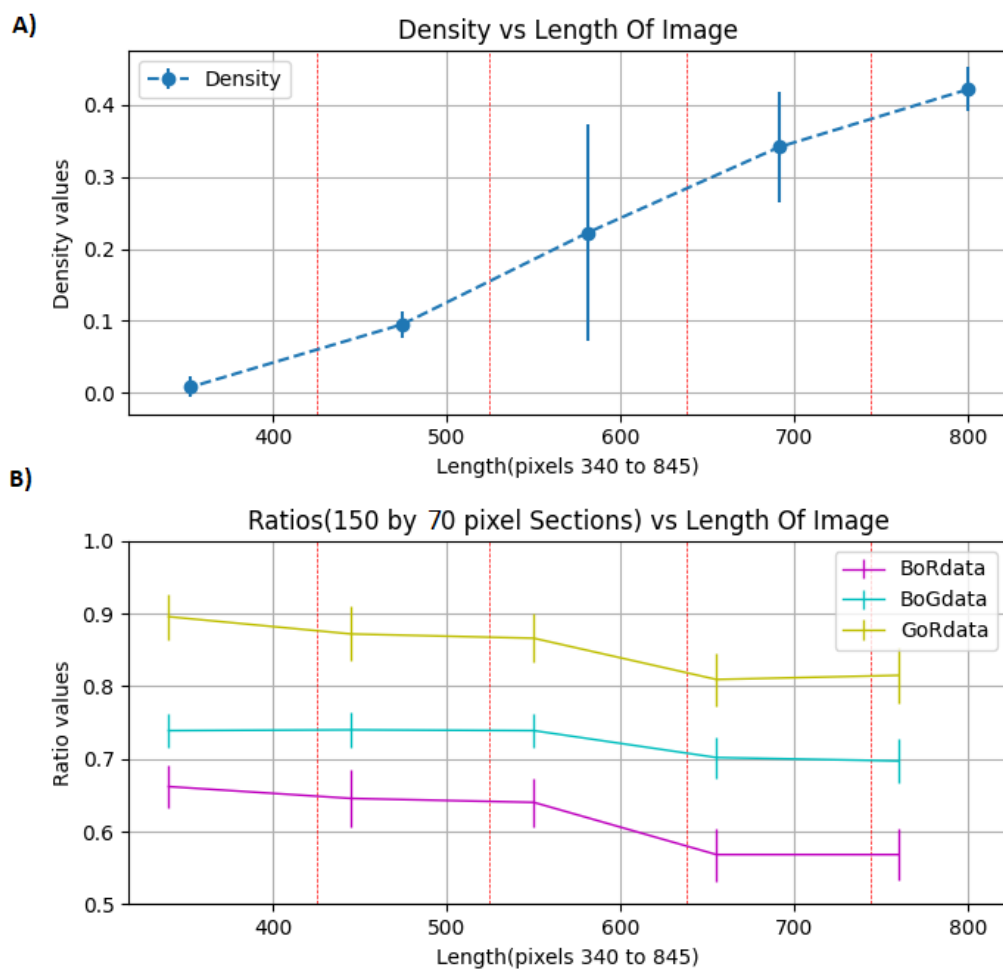
Figure 3.5: **Mean Dust Density and Color Ratios for Each Region.** Averaged dust density (A) and color ratios (B) are derived for each region along the microscope slide. The standard deviation is shown by vertical bars.

dispersion previously discussed. The standard deviations of the reflectance ratios of these 5 regions is of the same magnitude as the deviations of the multiple section evaluations. BoR and GoR have a standard deviation of about 0.036, while BoG has a deviation of about 0.026.

The Density plotted against the ratio values for each region shows a negative sloped trend for all three ratio profiles(Figure 3.6). This plot shows that the reflectance color ratios from an image are a valid method to measure the dust coverage of a dusty surface. This is particularly useful when the imaging spatial resolution is not sufficient in distinguishing the surface texture. Note that the background surface used in this result is white. Therefore, the ratio differences between dust-free and dust-covered regions are of the order 10-20%—much higher than the approximate 6% in Yan et al., 2019. In future work, data can be collected observing the ratios with a dark background similar to lunar rocks and with a background composed of the same material as the dust. These experiments will provide critical calibration information to analyze existing and future images from the surfaces of airless bodies when studying the dust deposition and the nature of dust mobilization.
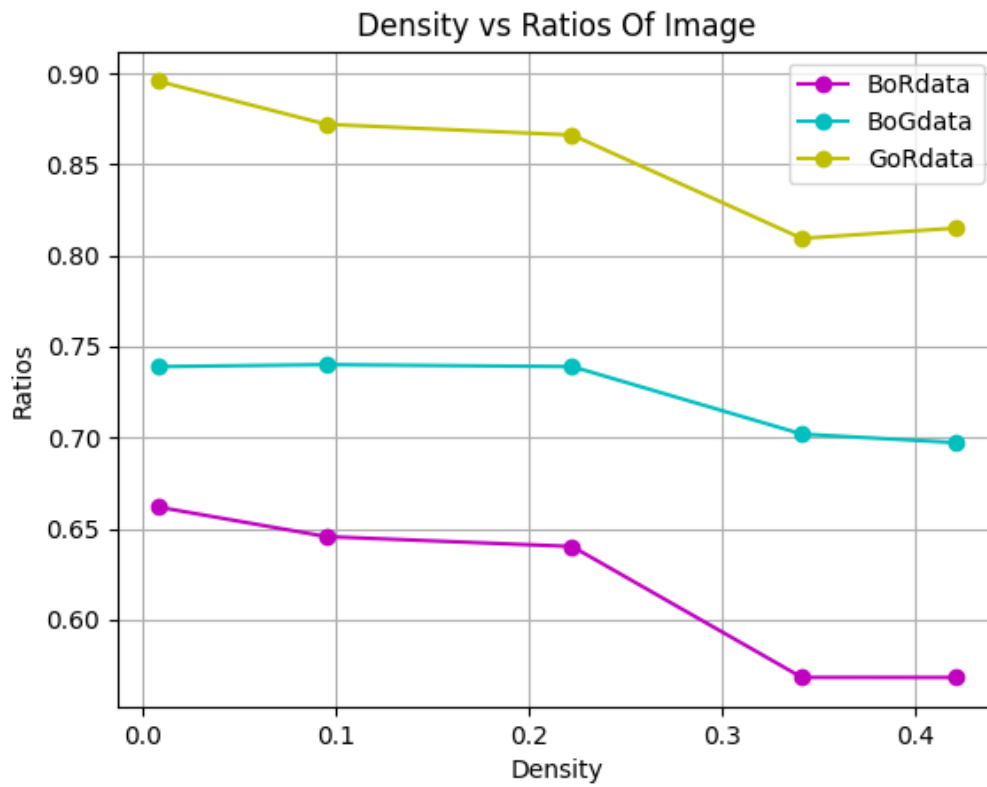
Figure 3.6: **Dust Density vs. the Reflectance Ratios.** The derived ratios are shown as a function of the dust density derived from microscope imaging to give an understanding about the correlation between ratio values and dust coverage.

Chapter 4

Conclusions and Future Studies

Dust lofting can tamper with many exploratory and scientific efforts on airless bodies, and a better understanding of dust mobilization is needed to help prepare missions in the future. Laboratory experiments have revealed many of the mechanisms behind electrostatic dust lofting, but more in situ studies are needed to support them. The main goal of this work was to validate the methods introduced by Yan et al. (2019) to quantify dust coverage using reflectance color ratios derived from color images. Our experiment used three physical color filters to take R, G, and B images of 5 regions of dustiness on a microscope slide. The reflectance ratios were derived for each region and compared to an analysis of the dust coverage based on microscope images. Combining these two independent measurements, we confirmed the remote sensing methods proposed in Yan et al., 2019 to evaluate the correspondence between reflectance color ratio and dust coverage on a surface.

With a white solid background, the reflectance ratios of dust were highest approaching unity in regions lacking dust, and lowest in regions with the highest dust density. Our quantitative results show a clear trend that the reflectance color ratios decrease with increasing dust density. These results are wholly consistent with the results from Yan et al., 2019. Our results show dust surface coverage ranges from 0.8% to 42.2%. The corresponding reflectance color ratio values are listed in Table 3.2. The difference in BoR values in dusty and dust-free regions are the most significant, which is also consistent with published results[15]. These values confirm the trend, and the standard deviation revealed higher deviations in regions slightly covered, but not fully blanketed, by dust,

likely caused by local coverage inhomogeneity.

By plotting the reflectance color ratio values as a function of dust coverage, we confirmed the assumption adopted by Yan et al., 2019, that lower color ratios correspond to higher dust density. This is valid specifically for dust on a light-color surface, but the behavioral trend of the color ratios should remain similar with different backgrounds. In other words, based on microscope image analysis, our results provide a preliminary "calibration curve" that can be applied to future quantitative analysis of dust deposition distribution based on remote sensing datasets.

To further our understanding, we plan to collect data with a darker background color, and with a solid surface composed of the same material as the dust. Determining how the ratios respond to dust coverage in these environments will help to examine the practicality and the limitations of this method of evaluating dust deposition on the surfaces of airless bodies such as the moon.

We also plan to electrostatically loft dust onto the surface of a microscope slide and perform the same analysis to examine the dust distribution with a more natural dust deposition mechanism. This remote sensing approach cannot measure the charges and phenomena of the lofting, but it can be used in tandem to monitor dust density and observe the effects of dust lofting in the laboratory and in space.

Bibliography

[1] J. E. Colwell, S. Batiste, M. Horńyi, S. Robertson, and S. Sture, "Lunar surface: Dust dynamics and regolith mechanics," <u>Review of Geophysics</u>, vol. 45, pp. 1–23, 2007.

[2] J. Rennilson and D. Criswell, "Surveyor observations of lunar horizon-glow," <u>The Moon</u>, vol. 10, pp. 121–142, 1974.

[3] I. G. Bethell, J. W. H. III, and C. M. Pieters, "Spectral properties, magnetic fields, and dust transport at lunar swirls," <u>Icarus</u>, vol. 212, pp. 480–492, 2011.

[4] M. Robinson, P. Thomas, J. Veverka, S. Murchie, and B. Carcich, "The nature of ponded deposits on eros," <u>Nature</u>, vol. 413, pp. 396–400, 2001.

[5] J. Colwell, A. Gulbis, M. Horńyi, and S. Robertson, "Dust transport in photoelectron layers and the formation of dust ponds on eros," <u>Icarus</u>, vol. 175, pp. 159–169, 2005.

[6] B. Smith, L. Soderblom, and et al., "Encounter with saturn: Voyager 1 imaging science results," <u>Science</u>, vol. 212, pp. 163–191, 1981.

[7] B. Smith, L. Soderblom, and et al., "A new look at the saturn system: the voyager 2 images," <u>Science</u>, vol. 215, pp. 504–537, 1982.

[8] G. Morfill, E. Grün, C. Goertz, and T. Johnson, "On the evolution of saturn's "spokes": theory," <u>Icarus</u>, vol. 53, pp. 230–235, 1983.

[9] C. Mitchell, M. Horńyi, O. Havnes, and C. Porco, "Saturn's spokes: Lost and found," <u>Science</u>, vol. 311, pp. 1587–1589, 2006.

[10] X. Wang, J. Schwan, H. Hsu, E. Grün, and M. Horńyi, "Dust charging and transport on airless planetary bodies," <u>Geophysical Research Letters</u>, vol. 43, pp. 6103–6110, 2016.

[11] A. Dove, M. Horányi, S. Robertson, and X. Wang, "Laboratory investigation of the effect of surface roughness on photoemission from surfaces in space," <u>Planetary and Space Science</u>, vol. 156, pp. 92–95, 2018.

[12] N. Hood, A. Carroll, R. Mike, X. Wang, J. Schwan, H.-W. Hsu, and M. Horányi, "Laboratory investigation of rate of electrostatic dust lofting over time on airless planetary bodies," <u>Geophysical Research Letters</u>, vol. 45, pp. 13,206–13,212, 2018.

[13] A. Carroll, N. Hood, R. Mike, X. Wang, H. W. Hsu, and M. Horńyi, "Laboratory measurements of initial launch velocities of electrostatically lofted dust on airless planetary bodies," <u>Icarus</u>, vol. 352, pp. 1–6, 2020.

[14] N. Hood, A. Carroll, X. Wang, and M. Horányi, "Laboratory measurements of size distribution of electrostatically lofted dust," Icarus, vol. 371, 2022.

[15] Q. Yan, X. Zhang, L. Xie, D. Guo, Y. Li, Y. Xu, and et al., "Weak dust activity near a geologically young surface revealed by chang'e-3 mission," Geophysical Research Letters, vol. 46, pp. 9405–9413, 2019.

[16] D. Criswell, "Horizon-glow and the motion of lunar dust." in: Grard, R.J.L. (Ed.). Photon and Particle Interactions with Surfaces in Space, (Springer, New York), pp. 545-556, 1973.

[17] ISO, "Thermal insulation — heat transfer by radiation — physical quantities and definitions." ISO Catalogue, 1989. Edition 1.

[18] T. Edelmann, "Firecapture." Downloaded from Vendor Site. http://www.firecapture.de/.

[19] Ocean-Insight™, "Ws-1 reflectance standards operating instructions." Download from Vendor Site. https://www.oceaninsight.com/globalassets/catalog-blocks-and-images/manuals–instruction-old-logo/sampling-accessories/ws-1-reflectance-standard.pdf.

[20] Meade-Instruments™, "Imaging color filter lrgb set (2")." Vendor Site. https://www.meade.com/catalog/product/view/id/567/s/imaging-color-filter-lrgb-set-2/.

[21] X. Ren, C. Li, J. Liu, F. Wang, J. F. Yang, E. Liu, and et al., "A method and results of color calibration for the chang'e-3 terrain camera and panoramic camera," Research in Astronomy and Astrophysics, vol. 14, pp. 1557–1566, 2014.

[22] J. R. Gaier, S. Ellis, and N. Hanks, "Thermal optical properties of lunar dust simulants and their constituents," Atmospheric and Space Environments Conference, vol. 3rd, 2011.